*J. Fluid Mech.* (1991), *vol.* 230, *pp.* 183–208
*Printed in Great Britain*



# Experimental investigation of coherent structures in turbulent boundary layers

By C. E. WARK AND H. M. NAGIB
Fluid Dynamics Research Center, Illinois Institute of Technology, Chicago, IL, 60616, USA

(Received 12 January 1990 and in revised form 22 February 1991)

The events which are responsible for strong Reynolds-stress production in the near-wall region of a bounded turbulent shear flow have been investigated in a turbulent boundary layer at a Reynolds number based on momentum thickness of $Re_\theta = 4650$. The coherent structures associated with the production process have been studied using the quadrant detection technique. All three velocity components were measured in a three-dimensional sampling volume about the point of detection. The conditional ensemble-averaged velocity field associated with the detection of a sweep or an ejection is presented and compared with non-conditioned space–time correlations. Conditional space–time probability density distributions were calculated at all measurement locations based on the occurrence of a Reynolds-stress-producing event at the detection point. The resulting three-dimensional representation of the conditional probability demonstrates that a significant fraction of the events are relatively large in scale, that a hierarchy of sizes exists and that there is a link between the outer flow and the 'bursting' process. However, many investigators have shown that the 'bursting' frequency scales with wall variables. Therefore all indications suggest that the scales are generated by a wall-layer mechanism but grow to sizes and convect with velocities scaling with the outer layer.

## 1. Introduction

Among the interests of current researchers in the study of turbulent boundary layers are the basic turbulence regenerative mechanism and attempts at control of some aspect of the turbulence. Research is largely focused on identifying dominant structures occurring in the flow field and the nature of the interaction between two distinct regions of the turbulent boundary layer: the inner and outer regions. Fundamental understanding of this basic flow field would be considered a major step in the subject of turbulence, in view of its importance to all wall-bounded shear flows that are ever present in engineering problems. The belief that the turbulent boundary layer is not just simply a random collection of events, but is indeed composed of coherent motions (at least a significant fraction of the time), is extensively documented, but the sizes, scaling, origin etc. of these coherent motions are the subject of many current investigations.

### 1.1. *Low-speed streaks*

One distinct feature of the turbulent boundary layer visually observed by Kline *et al.* (1967) and Corino & Brodkey (1969) among others, is low-speed streaks. A distinct characteristic of low-speed streaks as described by Kim, Kline & Reynolds (1971) is the bursting process. Briefly summarized, bursting occurs in three stages: (i) lift-up of low-speed streaks; (ii) growth of an oscillatory motion; (iii) breakup of the

oscillatory motions followed by a more quiescent flow. The occurrence of low-speed streaks and the insensitivity of the spanwise spacing of the streaks to Reynolds number is documented by Smith & Metzler (1983) for the range $740 < Re_\theta < 5830$. Many independent investigations have found that the spanwise spacing of streaks when normalized by inner variables is roughly $\lambda_s^+ = 100$. The breakup of the streak results in fluid being ejected very violently from the wall region into the outer flow. However, the visual observation of this ejection process provides little quantitative information; thus, several burst detection techniques relying on velocity measurements have been introduced.

### 1.2. *Burst detection techniques*

Rao, Narasimha & Narayanan (1971) band-pass filtered the streamwise velocity signal to identify regions of energetic activity. Lu & Willmarth (1973) used both a $u$-level technique and a quadrant technique. The $u$-level technique counts a burst when the fluctuating streamwise velocity falls below a certain threshold with respect to the long-time r.m.s. value of the streamwise velocity. The quadrant technique sorts the $u-v$ signal into quadrants based on the signs of the individual $u'(t)$ and $v'(t)$ signals, where $u'(t)$ and $v'(t)$ are the time-dependent streamwise and normal velocity fluctuations. The Reynolds stress-producing events (negative $u'(t)\,v'(t)$ events) fall into quadrants two ($u'(t) < 0; v'(t) > 0$) and four ($u'(t) > 0; v'(t) < 0$), hereafter referred to as Q2 and Q4 events respectively. It is also helpful to note here that a Q2 event is regarded as an ejection while the Q4 event is referred to as a sweep.

A widely used technique introduced by Blackwelder & Kaplan (1976) relies on the magnitude of the short-term r.m.s. of a fluctuating signal compared to the long-term r.m.s. value for the same signal. The VITA technique (Variable Interval Time Averaging) computes a short-term r.m.s. value for the streamwise velocity component (or temperature signal in some cases) for a specified length of time. If the short-term r.m.s. value is above a specified threshold with respect to the r.m.s. value for the entire time series, then a burst is counted. Later Chen & Blackwelder (1978) added a slope condition as well so that only events with an accelerating streamwise velocity component were counted. Without the slope condition it can be shown that the VITA technique mixes different types of events.

Recently at IIT, Guezennec (1985) used a shear-stress detection method at the wall to identify bursts. When the fluctuating streamwise shear stress ($\tau_x'$) is above a given threshold ($+k_x$) with respect to the long-term r.m.s. ($\tau_{x_{\rm ms}}'$) a sweep motion is detected. Likewise when $\tau_x' < -k_x \tau_{x_{\rm ms}}'$ an ejection motion is identified.

Bogard & Tiederman (1986) performed an evaluation of the effectiveness of several of the above-mentioned techniques by comparison with the results of a visual study. They found varying degrees of effectiveness of the various techniques and also found them to be highly dependent on the user-specified parameters. The results of their study indicate that the quadrant technique was the most reliable in the sense that it had a high probability of detecting ejections and a low probability of detecting false ejections. For single-sensor probes they conclude that the $u$-level technique was the most accurate.

Raupach (1981) found that sweep motions accounted for most of the Reynolds stress produced in the viscous sublayer, with ejections contributing more outside of the viscous sublayer. His result was consistent with those of Wallace, Eckelmann & Brodkey (1972) but inconsistent, for the sublayer region only, with the results of Lu & Willmarth (1973). Lu & Willmarth concluded that ejection motions were dominant for the entire region. As reported by them, 77% of the contribution to $-uv$ is by

ejection motions and 55% from sweep motions. The excess over 100% is due to the positive $uv$ contributions of outward (quadrant 1) and inward (quadrant 3) interactions ($u'(t) > 0; v'(t) > 0$ and $u'(t) < 0; v'(t) < 0$ respectively).

### 1.3. *Scaling of bursting frequency*

Lu & Willmarth (1973) using the quadrant detection technique in a turbulent boundary layer conclude that scaling with outer-flow variables ($U_\infty, \delta$) is appropriate, based on the better collapse of the ratio $f_{Q2}/f_{Q4}$ *vs.* $y/\delta$, as opposed to $y^+ = yu_\tau/\nu$. The frequency of Reynolds-stress events in the second and fourth quadrants are $f_{Q2}$ and $f_{Q4}$ respectively. This leads them to suggest that 'occurrence of bursting is determined by the outer flow conditions while the ensuing events near the wall after the burst begins are related to the wall-region variables'.

Using the narrow band-pass filter technique for a turbulent boundary layer Rao *et al.* (1971) also concluded that bursting frequency scales with outer variables, based on the better collapse of burst frequency, when non-dimensionalized with outer variables rather than inner variables. They further suggest that there is a strong coupling between the inner and outer flow based on the collapse of their data when using inner variables for the length parameter ($\nu/u_\tau$) and outer variables for the velocity parameter ($U_\infty$). Brodkey, Wallace & Eckelmann (1974) using the quadrant technique also determined that outer-flow scaling was appropriate, based on comparisons to Rao *et al.* (1971).

Blackwelder & Haritonidis (1983) using the VITA technique show that a sensor-length correction is needed owing to the spatial averaging effect of a hot-wire probe. Namely, the frequency observed will be too low owing to the averaging of the velocity signal over the length of the probe. Using this correction they determine that the burst frequency scales with inner variables and suggest that the results of Rao *et al.* (1971), which conclude that outer scaling is the appropriate choice, are in error owing to the spatial averaging effect.

Willmarth & Sharma (1984) also using VITA conclude that the burst frequency does not depend on the Reynolds number when scaled with inner variables. Guezennec (1985) using the VITA technique confirms the sensor-length correction and determines that inner scaling is the correct choice. Guezennec also established two important sampling criteria for proper detection of VITA events: the sampling frequency should be sufficiently high and the record length sufficiently long, $T_S^+ = T_S u_\tau^2/\nu < 4$ and $T_R^+ = T_R u_\tau^2/\nu > 8000$, where $T_S$ and $T_R$ are the time between data points (inverse sampling frequency) and time span of continuous data record respectively.

Kim & Spalart (1987) using the direct numerical simulation results for a turbulent boundary layer at low Reynolds numbers conclude that the bursting process scales with inner variables. Luchik & Tiederman (1987) using laser velocimetry in a water channel also confirm that inner scaling is the correct choice for the bursting phenomenon. Wark & Nagib (1988) using the quadrant, $u$-level and VITA detection schemes for both regular and flat-plate manipulated boundary layers, over a Reynolds-number range of $3000 < Re_\theta < 11000$, at several heights in the boundary layer ($15 < y^+ < 220$), conclude that bursting frequency scales with inner variables.

Alfredsson & Johansson (1984) introduced a mixed scaling which collapsed their burst frequency. More recently Sreenivasan (1987) illustrated that although the production of turbulent energy $-u'v'(\mathrm{d}U/\mathrm{d}y)$ scales with $y^+$, the Reynolds stress $-uv$ does not scale with inner variables but scales more precisely with the geometric mean of the inner and outer scales, i.e. mixed scales.

### 1.4. *Coherent structures*

The existence of coherent structures in turbulent boundary layers has been known for quite some time. Bakewell & Lumley (1967) using an eigenfunction decomposition of the fluctuating streamwise velocity component showed a dominant large-scale structure of the flow in the wall region composed of randomly occurring counter-rotating structures of long streamwise extent.

Blackwelder & Kovasznay (1972) present space–time correlations in a turbulent boundary layer for velocity signals obtained at the same streamwise and spanwise location but different vertical positions within the boundary layer. The $R_{uu}(\Delta x = 0, \Delta y, \Delta z = 0, \Delta t)$ correlation extends considerably outward into the boundary layer. The timescales obtained from the correlation show that the large structures persist for several boundary-layer thicknesses before losing their identity. The $R_{vv}(\Delta x = 0, \Delta y, \Delta z = 0, \Delta t)$ correlations however do not show the same spatial extent.

Using temperature as a passive scalar contaminant Chen & Blackwelder (1978) examined the large-scale motion in a turbulent boundary layer. Applying the VITA technique to the temperature signal revealed a sharp internal temperature front which extended throughout the entire boundary layer. A relation of this front to the bursting process at the wall was found. Studying the simultaneous temperature signals they found that the temperature fronts extend into the fully turbulent region as clearly identifiable structures.

Kreplin & Eckelmann (1979) presented space–time correlations for the fluctuating velocity components $u'$ and $w'$ and their associated gradients at the wall $\tau_x'$ and $\tau_z'$. The correlations were shown to decrease faster with increasing distance from the wall for the spanwise component as compared to the streamwise component. Their results imply the existence of counter-rotating structures with a spanwise spacing of approximately $\Delta z^+ = 50$ and a streamwise extent on the order of 1000 wall units. Blackwelder & Eckelmann (1979) suggest that the streamwise counter-rotating structures separated by approximately 50 wall units eject low-speed fluid away from the wall to the outer flow thereby causing the low-speed streaks.

Visual evidence of counter-rotating structures was first presented by Smith & Schwartz (1983). Although they were unable to determine the 'cause and effect relationship between low-speed streaks and counter-rotating structures' they did perceive that whenever a counter-rotating structure was detected, a low-speed streak was observed.

More recently Kasagi, Hirata & Nishion (1986) also visualized pseudo-vortical motions near the wall in a turbulent channel flow with a quasi-periodicity in the spanwise direction. Using the visual results of the hydrogen bubble technique, the instantaneous velocity components of $v$ and $w$ as well as the streamwise vorticity were computed. The centres of the vortical motions were found to occur between $y^+$ of 20 and 50.

Another distinct feature, in addition to wall-region counter-rotating structures, was visually observed by Head & Bandyopadhyay (1981) using smoke visualization. Hairpin vortices or vortex pairs that originate in the wall region and extend through a large part of the boundary layer, inclined at 40°–50° with respect to the horizontal, were seen to be significantly stretched and elongated with increasing Reynolds number. However, above $Re_\theta \approx 5000$ they were not able to adequately describe the resultant structure.

Very similarly Perry & Chong (1982) and Perry, Henbest & Chong (1986) proposed a model for the turbulent boundary layer which consists of a hierarchy of hairpins

at a fixed angle with respect to the flow. Their analysis demonstrates that these hairpins could be responsible for the mean vorticity, Reynolds stress and most of the energy-containing motions. A model for the growth of eddies within the hierarchy, consistent with the original ideas of Perry & Chong (1982) is outlined in Wark & Nagib (1989). Briefly summarized, the model is that joining of neighbouring structures would result in the destruction of their adjoining legs through cancellation of opposite-sign vorticity, thus leading to the growth of larger scales.

The counter-rotating structures presented above are small in scale with respect to recent results of Guezennec (1985) and Kim (1985). Guezennec experimentally measured $u'$, $v'$, $\tau_x'$ and $\tau_z'$ and applied the shear-stress detection technique. The conditionally averaged results show large-scale counter-rotating structures. The normal and spanwise scales were found to be of the order of half the boundary-layer thickness. The streamwise extent of the large scale extends for distances larger than the boundary-layer thickness.

Kim (1985) using the VITA detection technique for the data produced by the large-eddy simulation (LES) also finds large counter-rotating structures with a spatial extent of the order shown by Guezennec (1985).

### 1.5. *Objectives*

The objectives for the present investigation revolve around two important ideas: first to explore the interaction (if any) between large-scale structures and events occurring near the wall; secondly, to investigate the instantaneous structures involved in the 'bursting process'. These objectives are specifically outlined as follows. (i) Document the structures associated with strong Reynolds-stress production by experimentally measuring all three components of velocity in a three-dimensional grid with respect to a detection point. Specifically, to document a link between Reynolds-stress production near the wall and large-scale structures. (ii) Determine the scaling of an integral measure of this ensemble-averaged structure with Reynolds number. (iii) Using conditional probabilities, investigate the hierarchy of scales which make up the ensemble-averaged structure. This will give an indication of the differences in scale between the instantaneous and ensemble-averaged structure. (iv) Relate the conditionally averaged structure to the space–time correlations. Quantitative and qualitative comparisons will include the convection velocity of the resultant structure, inclination angles and extent of correlated region.

## 2. Experimental facilities and procedure

### 2.1. *Flow facility*

The measurements were performed in the Mark V. Morkovin wind tunnel at IIT. The tunnel is a closed-return wind tunnel with a series of honeycombs and screens which provide a turbulence intensity in the test section of less than 0.1% for speeds up to 35 m/s. The test section is 0.61 m by 0.91 m with a length of 5.88 m. The test plate is machined from aluminium and is located at a height of 30 cm from the floor of the test section. Sandpaper (24 grit), 20 cm in length, is placed on the test plate, directly downstream from the leading edge, to act as a fixed transition trigger. The mounting of the sandpaper is such that the substrate is flush with the upper surface of the test plate. A flexible ceiling allowed for a zero-pressure-gradient condition in the test section.

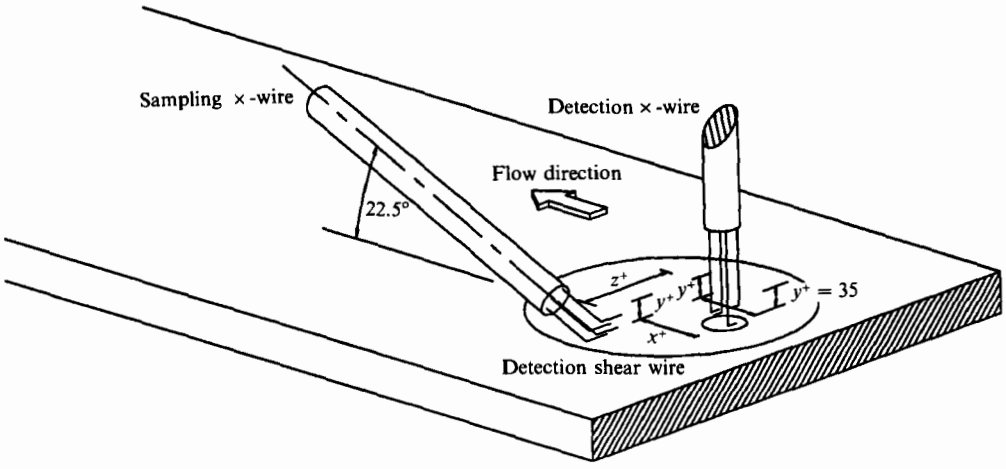


FIGURE 1. Schematic representation of measurement probes for three-dimensional mapping.

A schematic representation of the ×-wire probes used in the present study is shown in figure 1. Two orientations of the probe were used: one which allowed the simultaneous measurements of the streamwise and normal velocity components and the other which provided for the measurement of streamwise and spanwise velocities. To reduce the effects of probe interference the measurement volume was offset from the probe axis by 1 cm. In addition the 22.5° angle between probe body and axis of the ×-array (see figure 1) allowed for the positioning of the ×-array as closely as possible to the floor of the test section.

The simultaneous measurement of the streamwise and spanwise shear stress at the wall was performed using a V-shaped array of hot wires flush-mounted with the top surface of the Plexiglas plug described below. As described by Guezennec (1985) a small bore was machined in one of the two 10 cm diameter plugs to accommodate the Plexiglas plug, the top surface of which was coated with Ardyl (registered trademark of DuPont), a material having a very low heat conductivity. This smaller plug was allowed to rotate within the larger plug. Thus, since the larger plug could be positioned in any azimuthal direction, the proper alignment of the V-shaped shear sensor array with the flow, could be achieved over a limited spanwise distance. Jewellers broaches were secured in the Plexiglas plug and then ground flush with the top surface of the Ardyl coating. The hot wires were then soldered to the top surface of the broaches. The schematic representation of the wall plug is also shown in figure 1.

All wires were custom-made using 4 μm diameter tungsten wire. The wires were completely plated with a copper-sulphate solution except for a sensing length of approximately $l = 0.75$ mm or $l^+ = lu_\tau/\nu = 21$ for the $Re_\theta = 4650$ case which is the focus of this investigation. Boundary-layer profiles are presented in the range $3732 < Re_\theta < 5729$ for which $17 < l^+ < 26$. The plated wires are then silver soldered to the broaches of the hot-wire probe.

### 2.2. *Procedure*

To determine the effect of an error in the effective velocity cooling angle found during calibration on the results presented herein, a plus and minus 5% variation of this angle was assumed in the processing programs. It was seen that the conditional-

averaged structures and space–time correlations were insensitive to this angle. Also, the mean flow angle was calculated for each run and recalibration was performed if that angle was found to be greater than 2°. The voltages were thus calibrated to the effective cooling velocity angle found during calibration.

The V-shaped shear-sensor array was calibrated at $y^+ = 0$. The friction velocity, $u_\tau$, as a function of free-stream velocity, was known *a priori* by acquiring mean velocity profiles for several values of the free-stream velocity and performing Clauser fits to the profiles. The mean voltages of the shear-stress sensors were calibrated to this friction velocity. The values for the streamwise and spanwise shear stress ($\tau_x, \tau_z$) were subsequently calculated using $\tau_w = u_\tau^2 \rho$. Each time the plug was rotated and realigned with the flow a new calibration was performed.

For acquisition of boundary-layer profiles a single-sensor hot wire was used. One thousand points, sampled at 100 Hz, were acquired at 32 positions for each free-stream velocity and streamwise location of interest. The spacing between the measurements points increased as distance from the wall increased, owing to the velocity distribution of the boundary layer. Free-stream velocity and temperature were also sampled for monitoring free-stream conditions and hot-wire-voltage temperature compensation respectively.

As shown by Guezennec (1985), the sampling rate and record length must be such that $T_S^+ \leqslant 4$, and $T_R^+ > 8000$ to avoid errors in the VITA technique introduced by a digitization effect and insufficient record length respectively. In keeping with this a non-dimensional digitization rate and record length of $T_S^+ = 2$, $T_R^+ = 28000$ were used for the present investigation. Dimensionally this corresponds to 136530 points, for each of the acquired signals being sampled at 5612 Hz, giving a 24.3 s time record.

The mapping of the flow field for the quadrant detection scheme was performed as follows. The output from a fixed ×-wire probe (3.35 m downstream from the leading edge of the test plate) located at $(x^+, y^+, z^+) = (0, 35, 0)$ was acquired and later used for the quadrant detection scheme. Data were also acquired from a mapping ×-wire probe at several spatial positions $(x^+, y^+, z^+)$ with respect to the fixed detection probe, of a three-dimensional sampling grid. In addition the quantities $\tau_x$ and $\tau_z$ were also acquired at $x^+ = 0$, $y^+ = 0$, $z^+ = 0$. Therefore for each sampling grid point the following signals were acquired: $u$ and $v$ at $(0, 35, 0)$, $\tau_x$ and $\tau_z$ at $(0, 0, 0)$ and $u$ and $v$ at a given grid point. A similar experiment was performed, the only difference being that the orientation of the mapping ×-wire probe was changed to measure $u$ and $w$ at each grid point. Note: $x^+$ and $z^+$ refer to non-dimensional separation between detection and mapping ×-wire probes; whereas, $y^+$ refers to distance from the wall. Therefore, non-dimensional vertical spacing between the two ×-wire probes is $y^+ - 35$.

## 3. Results

### 3.1. *Boundary-layer profiles*

Boundary-layer profiles were acquired at five streamwise locations ($X$), as measured from the leading edge of the test plate, for three values of the free-stream velocity: $U_\infty = 10.8$, 12.9 and 16.9 m/s. This provided for overlapping of the Reynolds numbers in the range $3000 < Re_\theta < 9000$.

The self-similarity of the boundary layer is illustrated when presenting $u^+$ as a function of $y^+$ on linear-log coordinates (figure 2*a*). The mean streamwise velocity, $U$, and vertical height, $y$, have been normalized by inner boundary-layer scales ($\nu, u_\tau$), where $u_\tau$ was obtained from a Clauser fit to the data. The agreement of the profiles

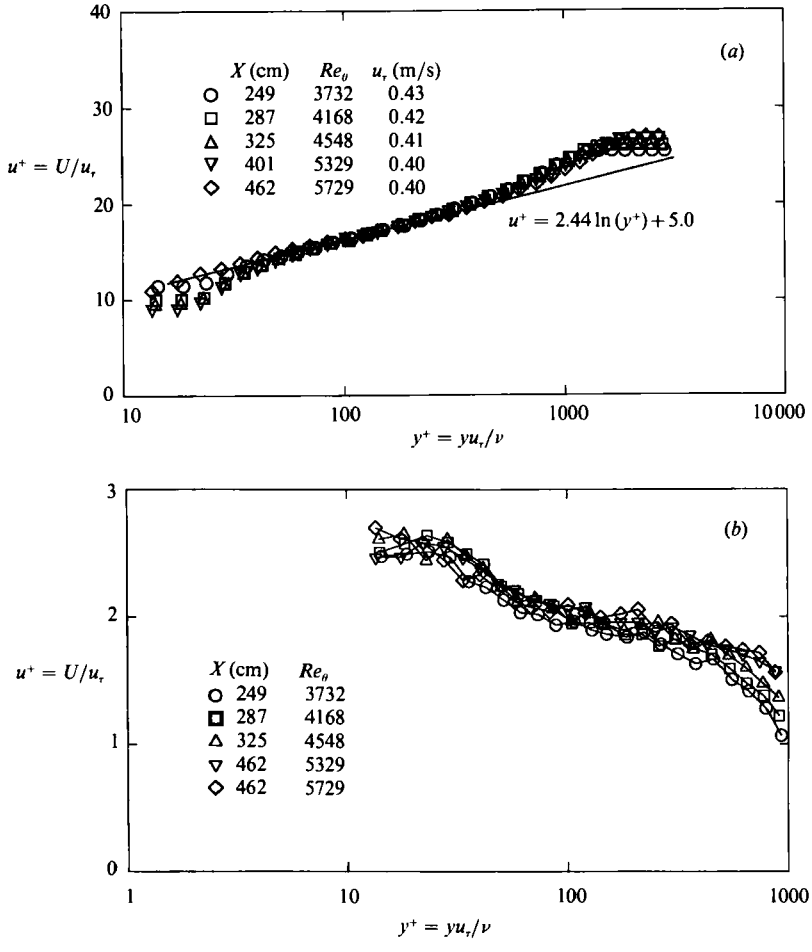


FIGURE 2. Comparison of (*a*) log law fit and (*b*) turbulence intensity profiles, normalized by wall variables at five downstream stations at 10.8 m/s.

at the various downstream positions with the law of the wall (shown as a solid line on the plots) represents the self-similarity of the boundary layers.

The associated turbulence intensity profile normalized by inner variables in semi-log coordinates is shown in figure 2(*b*). Again, no noticeable trend of the data is observed with downstream distance. The profiles for $U_\infty = 12.9$ and 16.9 (not shown) exhibit the same degree of collapse with streamwise location (see Wark 1988).

The skin-friction coefficient ($C_f$) and integral shape factors show excellent collapse for the overlapping ranges of Reynolds numbers and can be found in Wark (1988). The flow field in the experimental facility was verified to be two-dimensional and details of this can be found in Plesniak (1985). He presents momentum thickness, integral shape factors and skin-friction coefficient results as a function of both spanwise and streamwise location in the facility.

The results presented herein were acquired within the free-stream velocity and Reynolds number ranges presented above. The collapse of the shape factors and the self-similar boundary-layer profiles indicate an equilibrium turbulent boundary layer for $3000 < Re_\theta < 9000$.

### 3.2. *Space–time correlations*

Space–time correlations were computed in a turbulent boundary layer at several streamwise, spanwise and vertical positions for $Re_\theta = 4650$. The space–time correlation between two fluctuating quantities $\alpha$ and $\beta$ is defined by

$$R_{\alpha\beta}(x^+, y^+, z^+, t^+) = \frac{\overline{\alpha(x_0, y_0, z_0, t_0)\,\beta(x, y, z, t)}}{(\overline{\alpha'^2})^{\frac{1}{2}}(\overline{\beta'^2})^{\frac{1}{2}}},$$

where $(\overline{\alpha'^2})^{\frac{1}{2}}$ and $(\overline{\beta'^2})^{\frac{1}{2}}$ are the r.m.s. values of the time series at their respective positions of $x_0, y_0, z_0$ and $x, y, z$. The time delay and spatial separation between the measurement locations of the two quantities is non-dimensionalized by inner variables:

$$t^+ = \frac{(t-t_0)\,u_\tau^2}{\nu}; \quad x^+ = \frac{(x-x_0)\,u_\tau}{\nu}; \quad y^+ = \frac{(y-y_0)\,u_\tau}{\nu}; \quad z^+ = \frac{(z-z_0)\,u_\tau}{\nu},$$

where $(x-x_0)$, $(y-y_0)$ and $(z-z_0)$ are the spatial separations between $\alpha$ and $\beta$. The correlations were computed for values of $-440 \leqslant x^+ \leqslant 1320$, $55 \leqslant y^+ \leqslant 605$, and $0 \leqslant z^+ \leqslant 440$. The calculation of the correlation is based upon 136530 points sampled at 5612 Hz giving a time series of 24.3 s in length.

The quantities measured are the streamwise and spanwise wall shear stress, the streamwise and vertical velocity directly above the shear-stress sensor at $y^+ = 35$ and the three components of the velocity $(u, v, w)$ at several spatial positions or separations. For $z^+ = 0$, $R_{\tau_x u}(x^+, y^+, z^+ = 0, t^+)$ and $R_{vv}(x^+, y^+, z^+ = 0, t^+)$ correlations will be presented, and for $x^+ = 0$, $R_{\tau_x u}(x^+ = 0, y^+, z^+, t^+)$ correlations will be shown.

$R_{\tau_x u}(x^+, y^+, z^+ = 0, t^+)$ for $x^+ = 0$ and 1320 is shown in figure 3 for $55 < y^+ < 605$. The family of curves represents the various $y^+$ separations between the shear-stress sensor and the mapping $\times$-wire probe; the symbol on each curve corresponds to the $t^+$ associated with the maximum correlation. The correlation was computed for time delays of $-250 \leqslant t^+ < 250$ with $\Delta t^+ = 2$. With increasing $y^+$ the magnitude of the maximum correlation initially increases up to $y^+ = 110$ and then decreases for $y^+$ up to 605: this effect is somewhat puzzling at this time and is being investigated further. The $t^+$ for which the correlation is a maximum decreases with increasing $y^+$; an indication of an inclined correlated front.

The effect of streamwise separation on the family of curves is evident: for increasing $x^+$ the family of curves shifts towards increasing $t^+$ values. This gives an indication of the velocity with which the correlated front convects through the sampling volume. A slight decrease in the magnitude of the correlations is noted with increasing $x^+$; however, this decrease is small, suggesting a very long streamwise extent for the $R_{\tau_x u}$ correlation.

The space–time correlations of $R_{vv}(x^+, y^+, z^+ = 0, t^+)$ for $x^+ = -440$ and 440 are shown in figure 4. The two normal velocity signals were acquired from an $\times$-wire probe fixed at $y^+ = 35$ and the mapping $\times$-wire probe discussed above. For a spatial separation of $x^+ = -440$ the maximum correlation is observed at approximately $t^+ = -27$. Unlike the $R_{\tau_x u}$ correlation, the time for which the $R_{vv}$ correlation is a maximum ($t^+_{\max}$) does not decrease with increasing $y^+$. This suggests that unlike the $R_{\tau_x u}$ correlations the structures responsible for the $R_{vv}$ correlations are not inclined in the flow direction. At $x^+ = 440$, $t^+_{\max}$ is observed to be approximately equal to 27 for all $y^+$ positions and, with increasing streamwise separation, the magnitude of the correlation decreases and $t^+_{\max}$ increases. Again unlike the $R_{\tau_x u}$ correlation, the magnitude of $R_{vv}$ decreases rapidly and is very small for $x^+ = 1320$ (not shown).

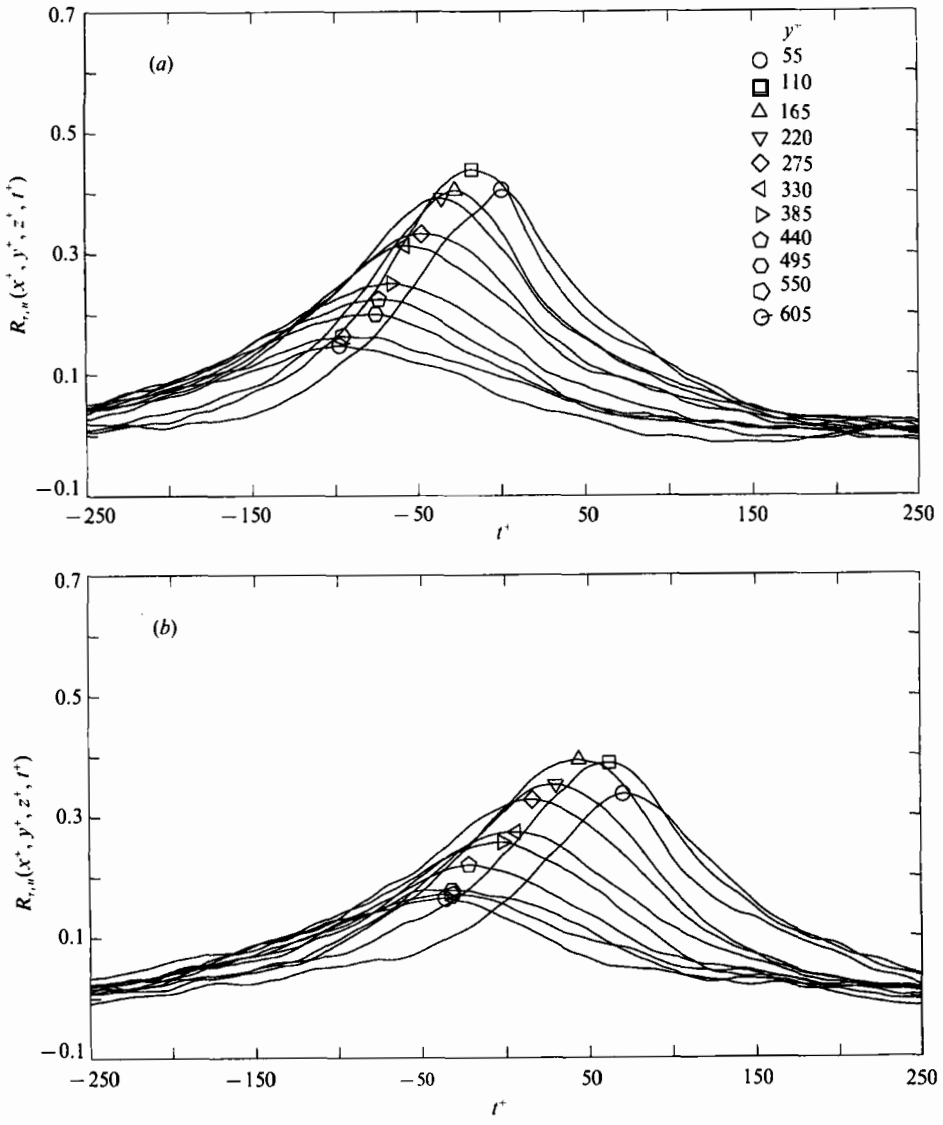


FIGURE 3. Temporal dependence of $R_{\tau_x u}$ correlations at $z^+ = 0$ and (*a*) $x^+ = 0$, and (*b*) $x^+ = 1320$ as a function of $y^+$.

The time delay of maximum correlation as a function of $x^+$ will provide the convection velocity of the structures responsible for the correlation. Figure 5(*a*) represents $t^+_{\max}$ as a function of $x^+$ for the several $y^+$ locations investigated using the $R_{\tau_x u}$ correlation results. The convection velocity $U_c$ is determined from the slope of the $t^+_{\max}$ *vs.* $x^+$ curves; specifically $U_c = u_\tau(\Delta x^+/\Delta t^+)$. The $t^+_{\max}$ values obtained from the $R_{vv}$ correlations are shown in figure 5(*b*). Only values for $y^+ \leqslant 275$ are shown owing to the very small levels of $R_{vv}$ for $y^+ > 275$; that is, for $y^+ > 275$, only background noise is reflected in the signal (see figure 4).

The convection speed ($U_c$) of the structures responsible for the $R_{\tau_x u}$ and $R_{vv}$ correlations are given in table 1 as a function of both $y^+$ and the $\Delta x^+$ range used in the calculation of $U_c$. For each $x^+$ range, the average convection velocity ($\overline{U_c}$) for all $55 \leqslant y^+ \leqslant 330$ is given below each column. For the $R_{\tau_x u}$ correlations the average ($\overline{U_c}$)

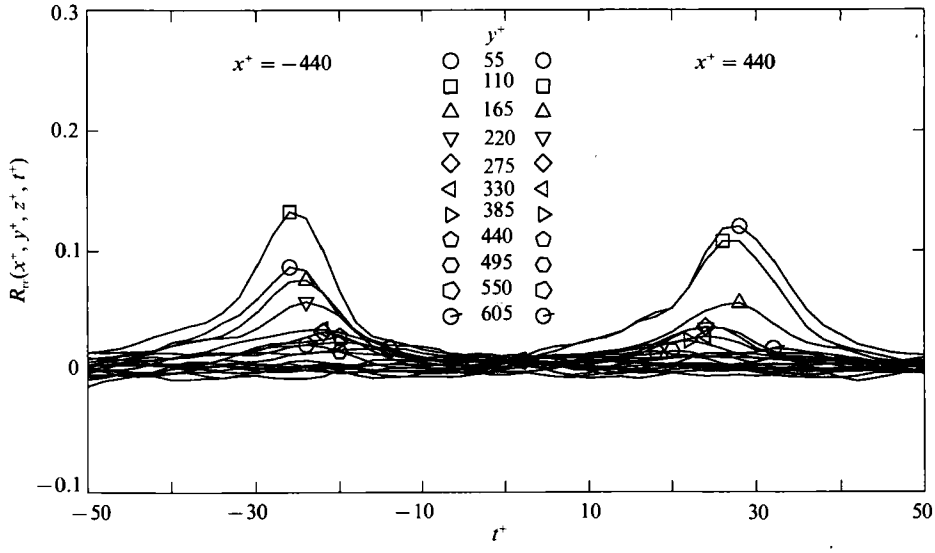


FIGURE 4. Temporal dependence of $R_{vv}$ correlations at $z^+ = 0$ for $x^+ = -440$ and $x^+ = 440$.

is insensitive to the chosen $x^+$ range. The $U_c$ values for each of the individual $y^+$ curves is also insensitive to the $x^+$ range, the largest deviation being a 13% decrease in $U_c$ for $y^+ = 55$ between $-440 \leqslant x^+ \leqslant 1320 (U_c/U_\infty = 0.69)$ and $-440 \leqslant x^+ \leqslant 440 (U_c/U_\infty = 0.60)$. The same conclusions are reached when looking at the $U_c$ results for the $R_{vv}$ correlations (bottom of table 1). At $y^+ = 220$, there is a 9% increase of $U_c$ between $-440 \leqslant x^+ \leqslant 880$ and $-440 \leqslant x^+ \leqslant 440$.

Using the data for $-440 \leqslant x^+ \leqslant 440$, the $y^+$ dependence on the convection velocity is shown in figure 5(*c*). The circles represent the results using the $R_{\tau_x u}$ correlation (figure 3) and the squares are the convection velocities determined from the $R_{vv}$ results (figure 4). The mean boundry-layer profile is shown as a solid line on the figure. The convection speed is observed to depend on $y^+$; namely as $y^+$ increases the convection velocity increases. More discussion on this is given in §4.2. There is scatter of the data; however, it is clear that $U_c$ is greater than the local mean velocity. Only results for $y^+ \leqslant 330$ and $y^+ \leqslant 275$ are given in table 1 and figure 5(*c*) for $R_{\tau_x u}$ and $R_{vv}$ correlations respectively: this is due to the increasing scatter with increasing $y^+$. Therefore, the above statement regarding $U_c$ being greater than the local mean is made only for $y^+$ range shown.

Also shown in table 1 are the inclination angles ($\gamma$; as defined by the insert in figure 5*c*) of the structures responsible for the $R_{\tau_x u}$ correlations. As mentioned above, the $t^+$ for which the correlation is a maximum decreases with increasing $y^+$. The inclination angle was calculated using the associated convection velocity; that is

$$\gamma = \tan^{-1}\left[\frac{\Delta y^+ \Delta t^+}{\Delta t^+ \Delta x^+}\right] = \tan^{-1}\left[\frac{\Delta y^+ u_\tau}{\Delta t^+ U_c}\right].$$

For $y^+ = 55$ and $-440 \leqslant x^+ \leqslant 440$, $\gamma = -9.7°$ was calculated using $\Delta y^+$ and $\Delta t^+$ between the $y^+ = 55$ and 110 curves at $x^+ = 0$ and $U_c = 0.69 U_\infty$. The average inclination angle ($\bar{\gamma}$) for $55 \leqslant y^+ \leqslant 330$ is given at the bottom of each column and is insensitive to the $x^+$ range used for the $U_c$ determination. It is found to be approximately 15°.

The spanwise influence on the $R_{\tau_x u}$ correlations is shown by a comparison of figure 6 ($z^+ = 110$) with figure 3(*a*) ($z^+ = 0$). As $z^+$ increases, the magnitude of both $R_{\tau_x u}$ and

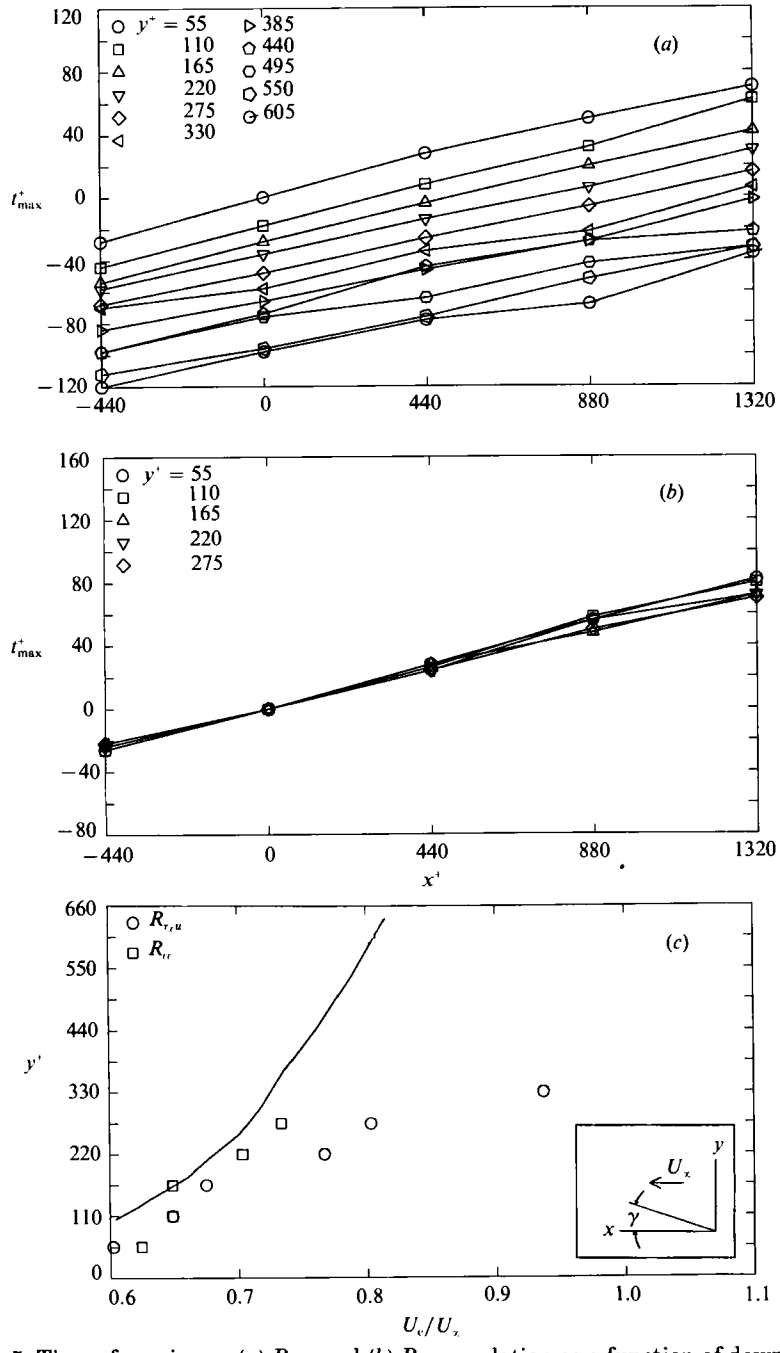


FIGURE 5. Time of maximum (*a*) $R_{\tau_x u}$ and (*b*) $R_{vv}$ correlation as a function of downstream distance for several heights. (*c*) Variation of convection velocity with height using both $R_{\tau_x u}$ and $R_{vv}$ space–time correlations.

$t^+_{max}$ decreases for all $y^+$ positions investigated, indicating a 'swept back' shape. This decrease in the magnitude of the correlation with spanwise separation is much faster than was seen for the streamwise separation results (comparison of figures 3*a* and 3*b*).

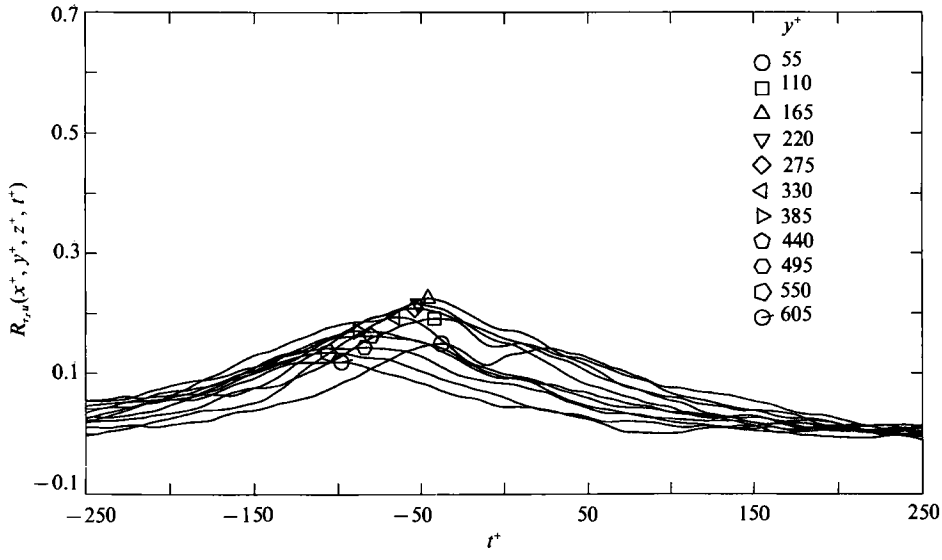


FIGURE 6. Temporal dependence of $R_{\tau_x u}$ correlations at $x^+ = 0$ and $z^+ = 220$.

| | $R_{\tau_x u}$ correlations | | | | | |
|---|---|---|---|---|---|---|
| | $-440 \leqslant x^+ \leqslant 1320$ | | $-440 \leqslant x^+ \leqslant 880$ | | $-440 \leqslant x^+ \leqslant 440$ | |
| $y^+$ | $\gamma$ | $U_c/U_\infty$ | $\gamma$ | $U_c/U_\infty$ | $\gamma$ | $U_c/U_\infty$ |
| 55 | 9.7° | 0.69 | 10.3° | 0.64 | 11.0° | 0.60 |
| 110 | 18.1° | 0.64 | 17.6° | 0.66 | 18.0° | 0.65 |
| 165 | 20.6° | 0.70 | 21.0° | 0.69 | 21.3° | 0.67 |
| 220 | 12.8° | 0.77 | 12.6° | 0.79 | 12.9° | 0.77 |
| 275 | 14.7° | 0.80 | 14.6° | 0.81 | 14.7° | 0.80 |
| 330 | 16.4° | 0.90 | 14.7° | 1.00 | 15.7° | 0.94 |
| | $\bar{\gamma} = 15.4°$ | | $\bar{\gamma} = 15.1°$ | | $\bar{\gamma} = 15.6°$ | |
| | $\overline{U_c} = 0.75U_\infty$ | | $\overline{U_c} = 0.77U_\infty$ | | $\overline{U_c} = 0.74U_\infty$ | |
| | $R_{vv}$ correlations | | | | | |
| | $-440 \leqslant x^+ \leqslant 1320$ | | $-440 \leqslant x^+ \leqslant 880$ | | $-440 \leqslant x^+ \leqslant 440$ | |
| $y^+$ | $U_c/U_\infty$ | | $U_c/U_\infty$ | | $U_c/U_\infty$ | |
| 55 | 0.62 | | 0.62 | | 0.62 | |
| 110 | 0.62 | | 0.61 | | 0.65 | |
| 165 | 0.70 | | 0.69 | | 0.65 | |
| 220 | 0.68 | | 0.64 | | 0.70 | |
| 275 | 0.72 | | 0.70 | | 0.73 | |
| | $\overline{U_c} = 0.67U_\infty$ | | $\overline{U_c} = 0.65U_\infty$ | | $\overline{U_c} = 0.67U_\infty$ | |

TABLE 1. Inclination angles and convection velocities of structures responsible for the $R_{\tau_x u}$ and $R_{vv}$ correlations

A schematic of a structure which could result in the long-time correlations discussed above is shown in Guezennec (1985) and Nagib & Guezennec (1986). Their schematic is based upon a conditionally averaged structure and depicts a 'large-scale' roller-type structure. Also consistent with their schematic are space–time correlations between the streamwise and spanwise component of velocity and can be found in Wark (1988).

### 3.3. *Ensemble-averaged quadrant detection results*

The quadrant detection technique, introduced by Lu & Willmarth (1973) requires the measurement of the streamwise and normal velocity components. The $u'(t)\,v'(t)$ product is split into quadrants based on the sign of the individual components: the detection function $D(t)$ is given below:

$$\text{Q4 (Sweep event)} \quad D(t) = \begin{cases} 1 & \text{if } u'(t) > 0,\ u'(t)\,v'(t) < -k_{\mathrm{Q}}\,u_{\mathrm{rms}}\,v_{\mathrm{rms}} \\ 0 & \text{otherwise,} \end{cases}$$

$$\text{Q2 (Ejection event)} \quad D(t) = \begin{cases} 1 & \text{if } u'(t) < 0,\ u'(t)\,v'(t) < -k_{\mathrm{Q}}\,u_{\mathrm{rms}}\,v_{\mathrm{rms}} \\ 0 & \text{otherwise,} \end{cases}$$

where the subscript rms denotes the root-mean-square value for the entire time series and $k_{\mathrm{Q}}$ is the quadrant threshold parameter.

For the present investigation $k_{\mathrm{Q}}$ was chosen to be equal to 3.0. The percentage of the $\overline{u'v'}$ product for the detected Q2 and Q4 events was approximately 30% and 15% of the total $\overline{u'v'}$ contribution from quadrants two and four respectively. The percentage of Q2 and Q4 events detected was approximately 6% and 2% of the total events in quadrants two and four. This corresponds to 1.8% and 0.7% of events in all quadrants.

Using an $\times$-wire probe to measure the streamwise and normal velocities in a three-dimensional sampling grid around a detection point, Guezennec showed that the ensemble-averaged structures associated with a Reynolds-stress-producing event were roller-type structures. These structures extend from the wall to $y^+ > 600$, had a spanwise width of approximately $z^+ = 600$ and a streamwise extent of several boundary-layer thicknesses. The spanwise velocity ($w$) was calculated using continuity, assuming a line of symmetry at $z^+ = x^+ = 0$. The data were taken on one side of the detection point only. Details of this investigation can be found in Guezennec (1985).

The present data were acquired at several grid positions on both sides of the detection point. The mapping $\times$-probe was positioned with respect to the detection probe at five streamwise ($x^+$), nine spanwise ($z^+$), and 11 vertical ($y^+$) locations. The values chosen for the mapping were ($x^+ = -440$ to 1320, with $\Delta x^+ = 440$; $y^+ = 55$ to 605, with $\Delta y^+ = 55$; and $z^+ = 0$ to 440, with $\Delta z^+ = 110$). A 24.3 s time record consisting of 136530 points for each of the six signals (mapping probe $u$ and $v$, detection probe $u$ and $v$ and wall shear stresses $\tau_x$ and $\tau_z$) was acquired at each of the grid points. The average values over the entire time record for each signal were subtracted from the time series and further processing was performed on the time-dependent fluctuating signals only.

The average perturbation streamwise and normal velocities ($\langle u \rangle$ and $\langle v \rangle$) associated with a detection were calculated for each grid point; that is,

$$\langle u \rangle = \overline{D(t)\,u'(t)} \quad \text{and} \quad \langle v \rangle = \overline{D(t)\,v'(t)}.$$

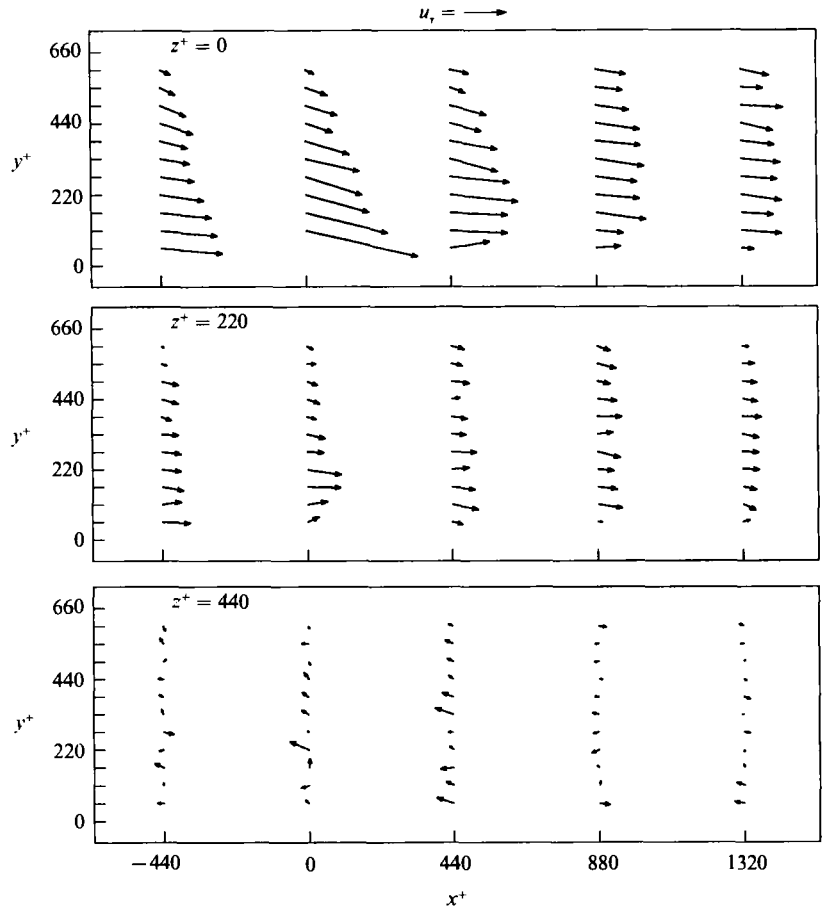


FIGURE 7. Perturbation velocity vector maps in the $(x^+, y^+)$-plane of increasing spanwise offset between detection and mapping probes for a Q4 detection at $(x^+, y^+, z^+) = (0, 35, 0)$. $Re_\theta = 4620$.

These perturbation velocities for each grid point are represented as $\langle u \rangle$, $\langle v \rangle$ velocity vectors in the $(x^+, y^+)$-plane (figures 7 and 8) for the three spanwise offsets of $z^+ = 0$, 220 and 440.

For both sweeps (figure 7) and ejections (figure 8) the maximum velocity vector magnitudes are found at $z^+ = 0$. For $z^+ = 220$ a definable structure is seen for the Q4 event only. The average structure associated with a sweep event is much stronger than that associated with an ejection of fluid from the wall region. At $z^+ = 440$ the velocity vectors for both the Q4 and Q2 events have reversed sign as compared with the $z^+ = 0$ results.

For the results presented, no attempt was made regarding spanwise 'centring' of events. Guezennec (1985) using a shear-stress detection technique 'centred' events by applying a maximum threshold on the magnitude of the spanwise wall-shear stress; that is, only events that were within a small deviation from $\tau_z' = 0$ and exceeded the streamwise wall-shear stress threshold were used in the ensemble-averaging process. This did not result in different conclusions regarding the relative strengths of high- and low-shear-stress events. A possible explanation for this is that the spatial resolution of the shear stress measurement probe was relatively large (100 wall units); thus, centring would have no effect on these results. It is expected that

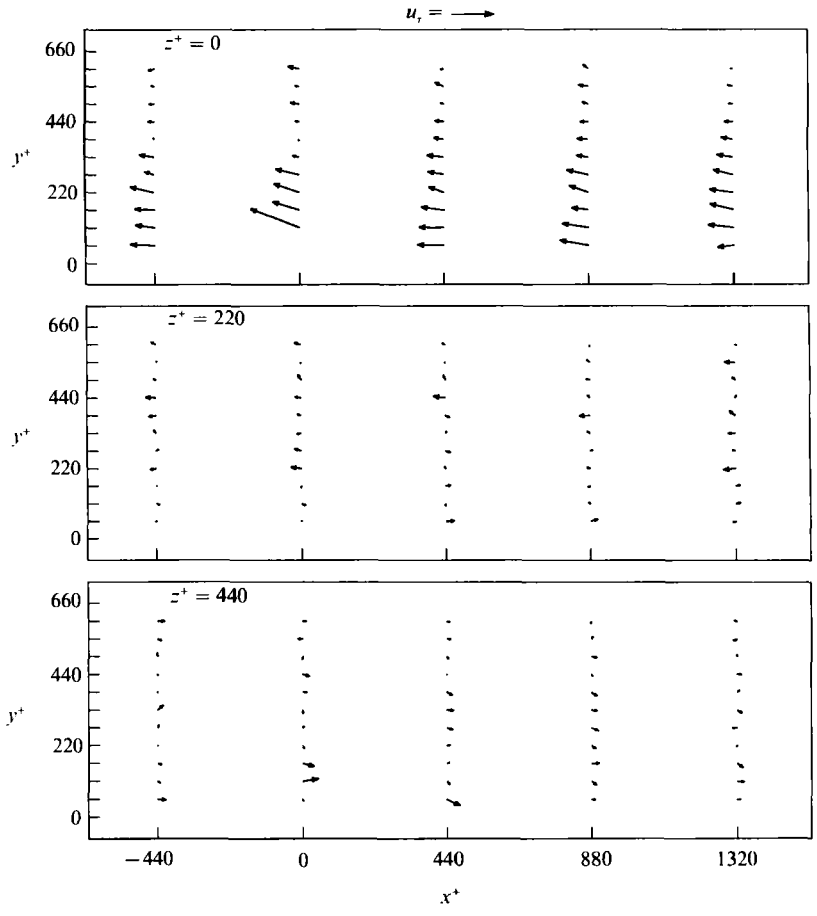


FIGURE 8. Perturbation velocity vector maps in the $(x^+, y^+)$-plane of increasing spanwise offset between detection and mapping probes for a Q2 detection at $(x^+, y^+, z^+) = (0, 35, 0)$. $Re_\theta = 4620$.

if the spanwise shear stress were measured with a smaller sensor or if the spanwise velocity component were measured directly above the wall, then the centring scheme would be successful. Johansson, Alfredsson & Kim (1987), point out that 'spanwise centering of the events is essential to obtain reasonable quantitative estimates of the associated Reynolds stress contributions...'. The lack of 'centring' is a possible explanation for the relatively weaker ensemble-averaged Q2 structure. However, in the following section, it will be shown that another contributing factor is that for this detection scheme at $Re_\theta = 4650$ a greater percentage of the Q4 events are 'large' in scale as compared with the Q2 events.

For the results presented in figure 9, the perturbation velocities for each grid point were averaged over the five $x^+$ and eleven $y^+$ positions for a given spanwise location. It is easily seen from these results that the magnitude of the conditionally averaged $u$ and $v$ velocity components are greater in magnitude for the sweep event than for the ejections. The maximum value for both the $u$ and $v$ components occurs at the detection point ($z^+ = 0$). Note: to investigate the two-dimensionality of the experimental set-up, the ensemble-averaged structure was found to be symmetric (by acquiring data on both sides of the detection point). This was expected; however, this does not imply that the instantaneous structure is symmetric. Note also that

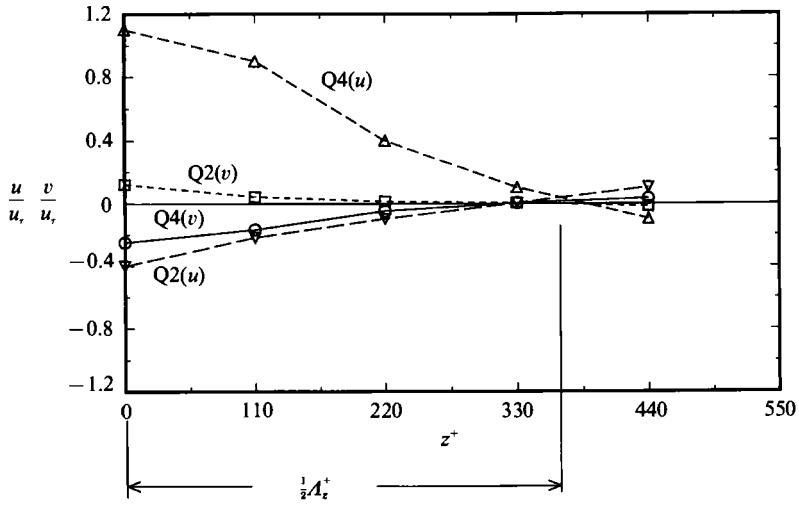


FIGURE 9. Spanwise variation of average streamwise and normal perturbation velocities associated with Q4 and Q2 events.

both the average Q4 and Q2 events have the same spanwise extent. An 'integral' measure of the spanwise extent of the Q4 and Q2 events is defined by $\Lambda_z$. Specifically $\Lambda_z$ is the $z^+$ location where $u/u_\tau \approx = 0$ (average between Q2 and Q4).

Furthermore, when detecting a Q4 event at $z^+ = 0$, a weak Q2 event is picked up for $z^+ > 350$ and vice versa. The magnitude of the 'second structure' is approximately one-third that of the structure at the point of detection. This is significant in the sense that the sweep and ejection events both have a quasi-periodicity in the spanwise direction. The results for the average $v$ also indicate this spanwise periodicity with a wavelength that is somewhat smaller than one but greater than one-half the wavelength for the streamwise component.

The measurement of the average perturbation streamwise and spanwise components of velocity were also performed for both the Q2 and Q4 events using an $\times$-wire probe oriented to obtain $u$ and $w$. The perturbation streamwise and normal velocity vector results presented above (figures 7 and 8) were incorporated with these measurements to construct the $v, w$ velocity vector maps shown in figures 10 and 11 for the Q4 and Q2 detections respectively.

For the Q4 event a clear sense of rotation is evident with the centre of a 'roller' structure at approximately $(z^+, y^+) = (275, 165)$ at $x^+ = -440$. Progressing downstream it is noted that the centre of the structure moves upward with increasing $x^+$: this is very pronounced for the Q4 event. For the Q2 case there is not a well defined large-scale rotating structure at $x^+ = -440$. At $x^+ = 0$, the sense of rotation is evident: this is also seen for the results at $x^+ = 440$; however, the magnitude of the velocity vectors is small. These results are in good agreement with the measured $v$ and calculated $w$ results of Guezennec (1985) and Nagib & Guezennec (1986) discussed previously. Again, as mentioned, no 'centring' of the individual structures was performed. Using the centre of the vortices to define a vertical inclination angle (defined in the same way as $\gamma$ on figure 5*c*) of the roller-type structures results in a 5.8° and 20° angle for the Q4 event for $-440 \leqslant x^+ \leqslant 0$ and $-440 \leqslant x^+ \leqslant 440$ respectively. This reflects a structure with increasing $\gamma$ (increasing curvature away from the wall with increasing streamwise distance). Since a rotating structure

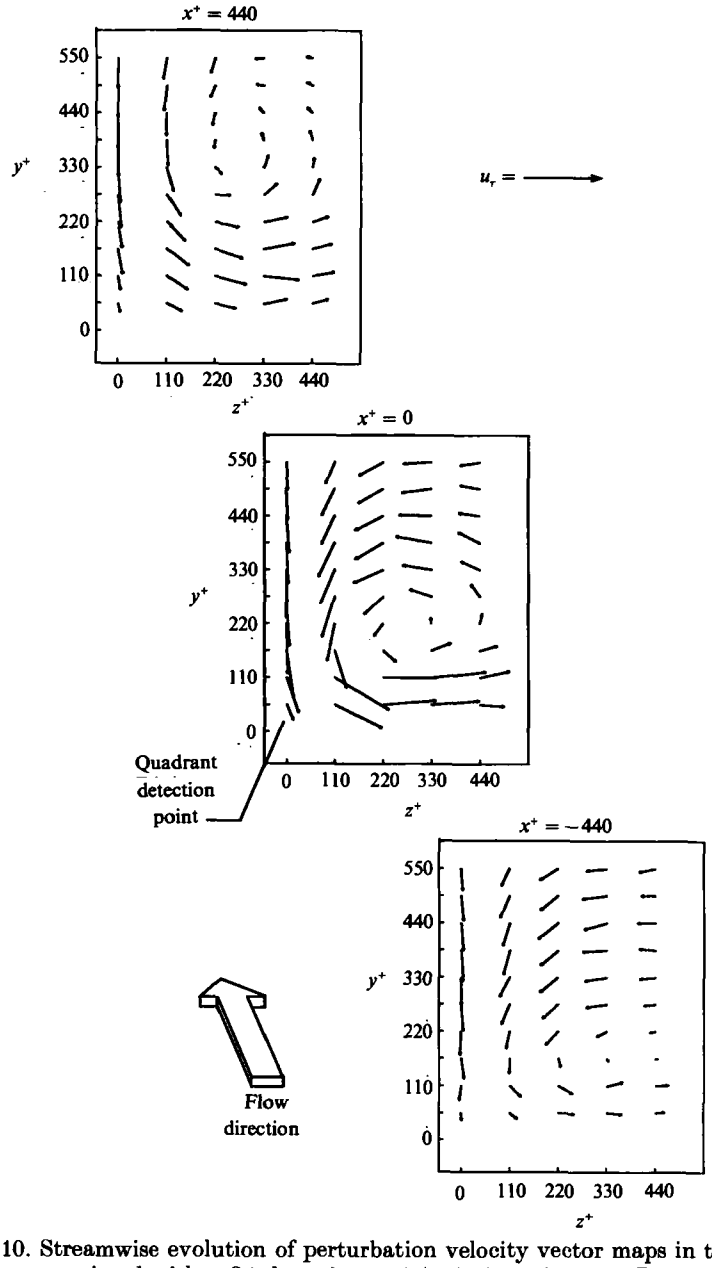


FIGURE 10. Streamwise evolution of perturbation velocity vector maps in the $(y^+, z^+)$-plane associated with a Q4 detection at $(x^+, y^+, z^+) = (0, 35, 0)$. $Re_\theta = 4620$.

is not observed at $x^+ = -440$ for the Q2 event, an angle of 12.2° is calculated for $-440 \leqslant x^+ \leqslant 0$ range only.

### 3.4. *Pseudo-instantaneous quadrant detection results*

The results discussed above are all based on the ensemble-averaged quantities for the perturbation velocities. Knowledge of the instantaneous field is more useful and interesting than of the mean field; however, the associated experimental limitations are numerous. The results presented in this section attempt to extract as much

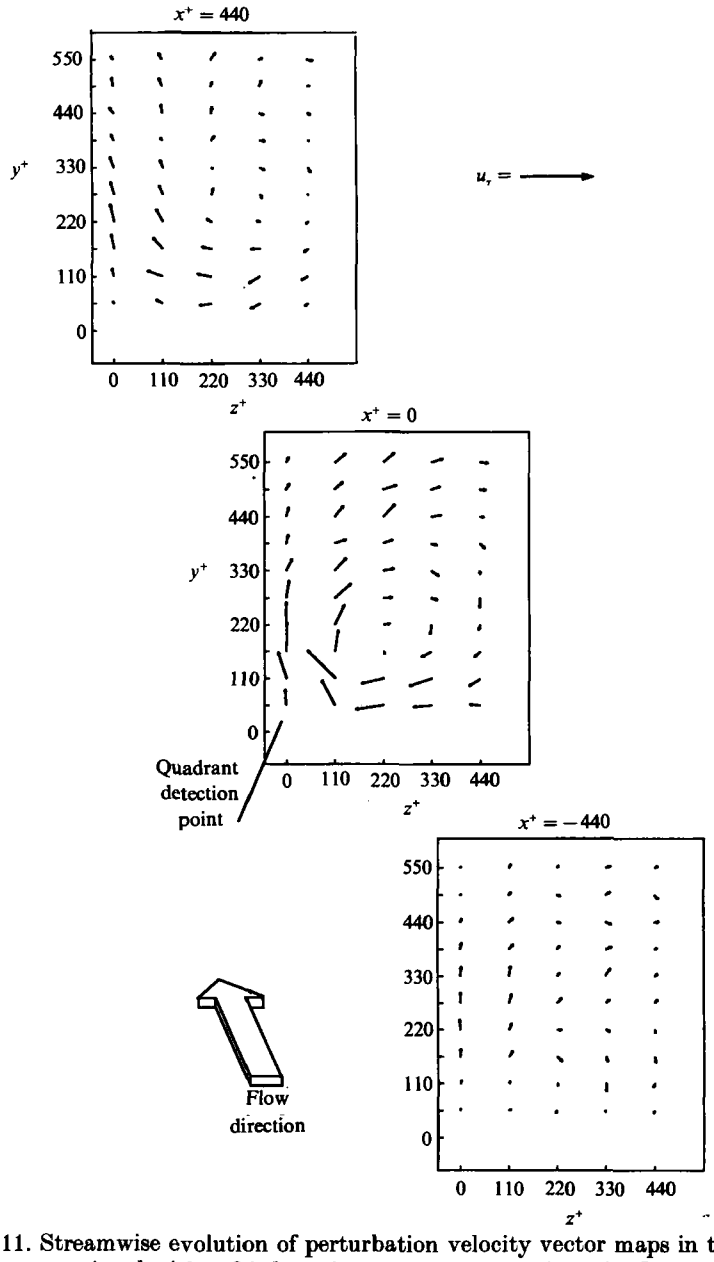


FIGURE 11. Streamwise evolution of perturbation velocity vector maps in the $(y^+, z^+)$-plane associated with a Q2 detection at $(x^+, y^+, z^+) = (0, 35, 0)$. $Re_\theta = 4620$.

information as possible from the present measurements regarding the instantaneous field.

The approach taken for the present results is based on the probability density distributions (p.d.f.) for the time between an event recognized at the detection point and an event observed at the mapping probe. For example, the p.d.f. of the time between a strong Q4 event ($k_Q = 3.0$) at the detection point $(0, 35, 0)$ and a Q4 event at $(440, 55, 0)$ ($k_Q = 0$) is shown in figure 12. The discrete bins of the p.d.f. are one sampling time ($t^+ = 2$) in width, where time is non-dimensionalized by inner

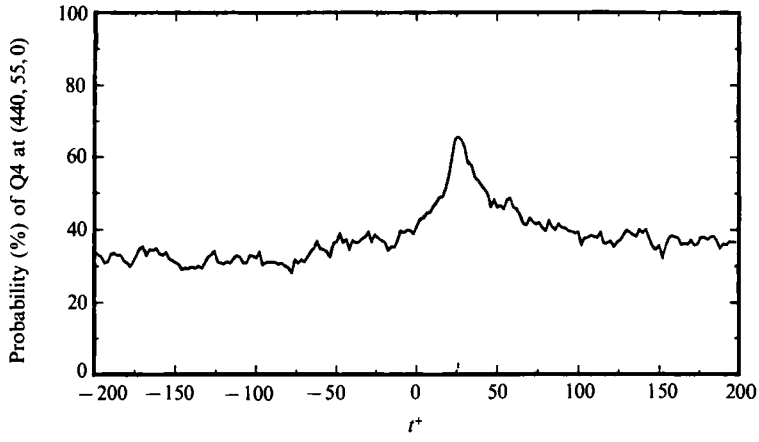


FIGURE 12. Probability density distribution of time between detection of a strong Q4 event ($k_Q = 3.0$) at $(x^+, y^+, z^+) = (0, 35, 0)$ and a Q4 event ($k_Q = 0$) at $(x^+, y^+, z^+) = (440, 55, 0)$.

variables, and the ordinate is given in percent: the $t^+ = 0$ point corresponds to the time of detection of an event at (0, 35, 0), for this example, a Q4 event. After the time of detection ($t^+ = 26$), a Q4 event is observed at (440, 55, 0) approximately 65% of the time that a Q4 event is detected at the detection point. The fact that the maximum probability occurs after the time of detection at a streamwise location downstream of the detection point represents the convection of the structures associated with a Q4 detection: this issue is addressed later in the section.

The maximum probability of 65% discussed with reference to figure 12 includes events which are correlated to the detection event and those which are uncorrelated. The uncorrelated results are related to the frequency of occurrence of a Q4 event ($k_Q = 0$) at a single point. To further explain this, two limiting cases will be discussed.

For the first case, consider that the detection and mapping probe were measuring at the same point; therefore, all events are correlated. In the second scenario, the mapping and detection probes are sufficiently far apart that the time series measured at the two probes are uncorrelated. For this case, the percentage of time that a Q4 event ($k_Q = 0$) is observed at the mapping probe while detecting a Q4 ($k_Q = 3.0$) event at the detection probe is simply the frequency of occurrence of a Q4 ($k_Q = 0$) event at any point in the flow field. Hence, the uncorrelated events or 'background' probability are a function of the spatial separation between the detection and mapping probes. A similar thought exercise can be performed for time separations between two points in the two time series. Doing this results in time dependence as well as a spatial separation dependence of the 'background' probability function. Even though the background probability is a function of both space and time, the correlated probability was determined by subtracting from the calculated probability a constant value equal to the probability associated with the frequency of occurrence of a Q4 or a Q2 event ($k_Q = 0$). For the Q4 case, the probability asymptotes to approximately 32% at $t^+$ values sufficiently far away from the detection time (see figure 12). Subtracting this value from all calculated probabilities gives a conservative estimate; that is, the probability of finding an event at a given point in the grid which is correlated with the detection point is greater than or equal to the value shown hereafter.

To obtain three-dimensional spatial information, probability density distributions were calculated for all discrete points in the measurement grid. The magnitude of the

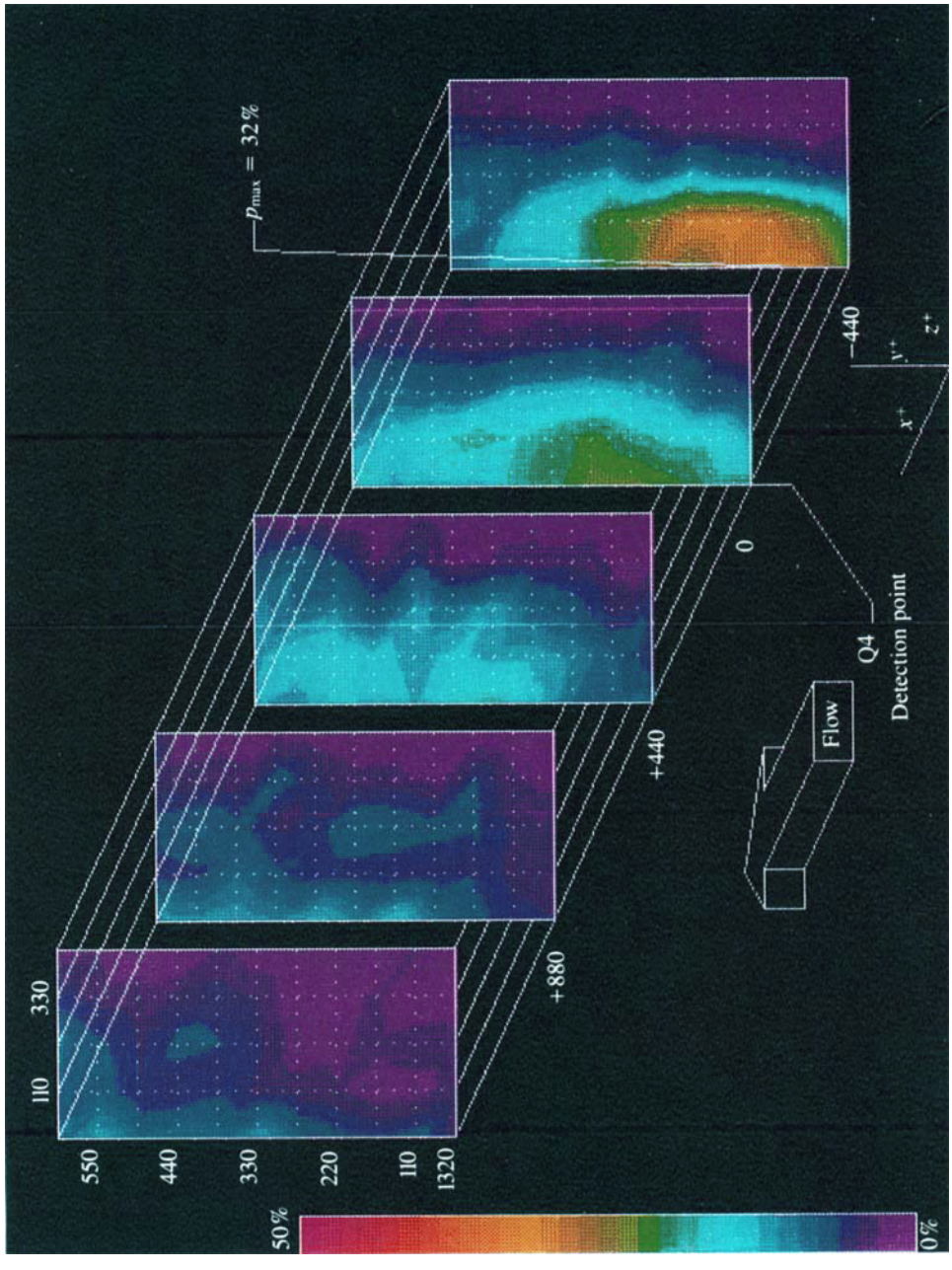


FIGURE 13. Spatial representation of the probability of observing a Q4 event ($k_Q$=0) $30t^+$ before the detection of a Q4 event at (0,35,0). $Re_\theta$ = 4650.

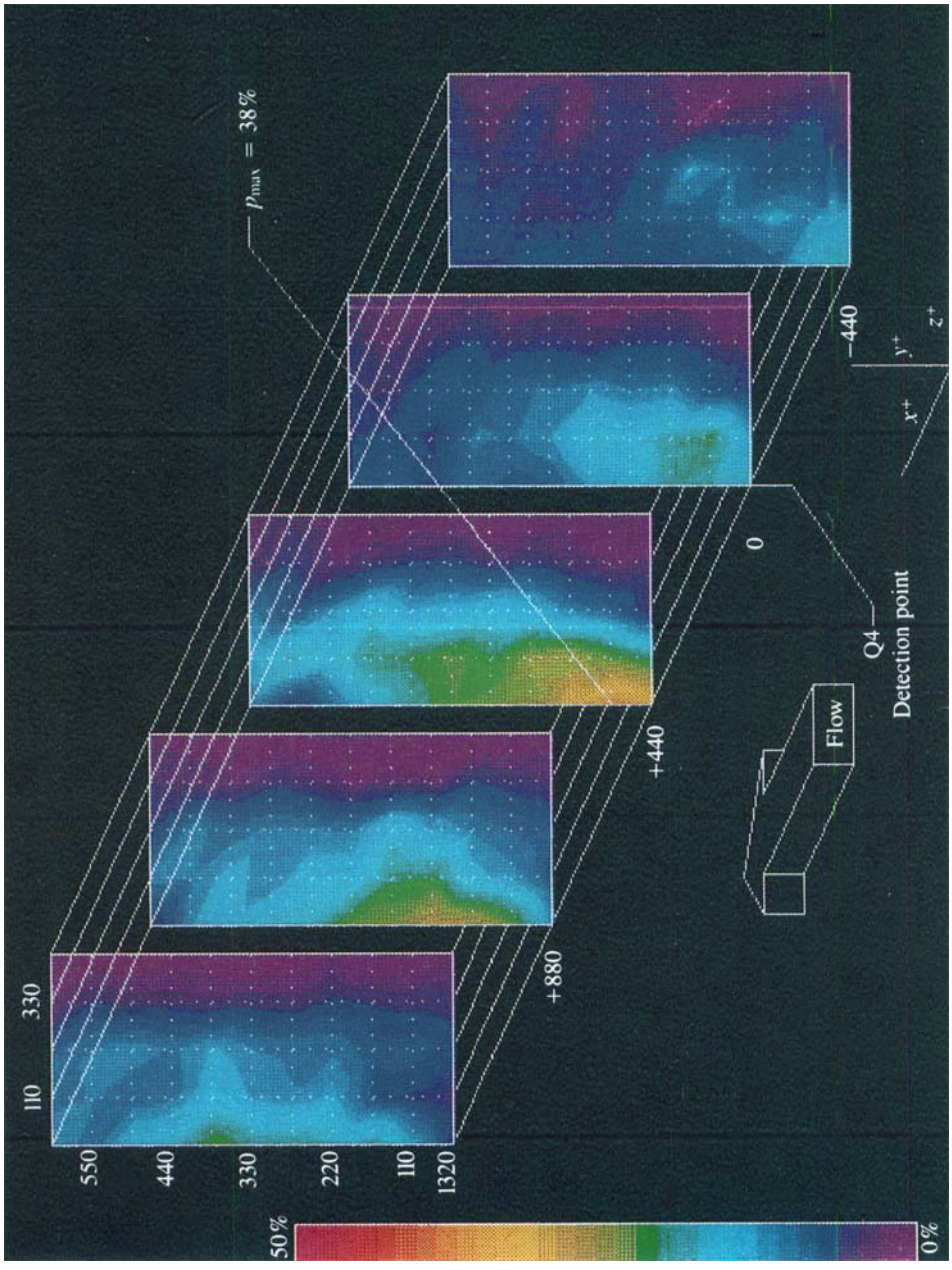


FIGURE 14. Spatial representation of the probability of observing a Q4 event ($k_Q$=0) $30t^+$ after the detection of a Q4 event at (0,35,0). $Re_\theta$ = 4650.

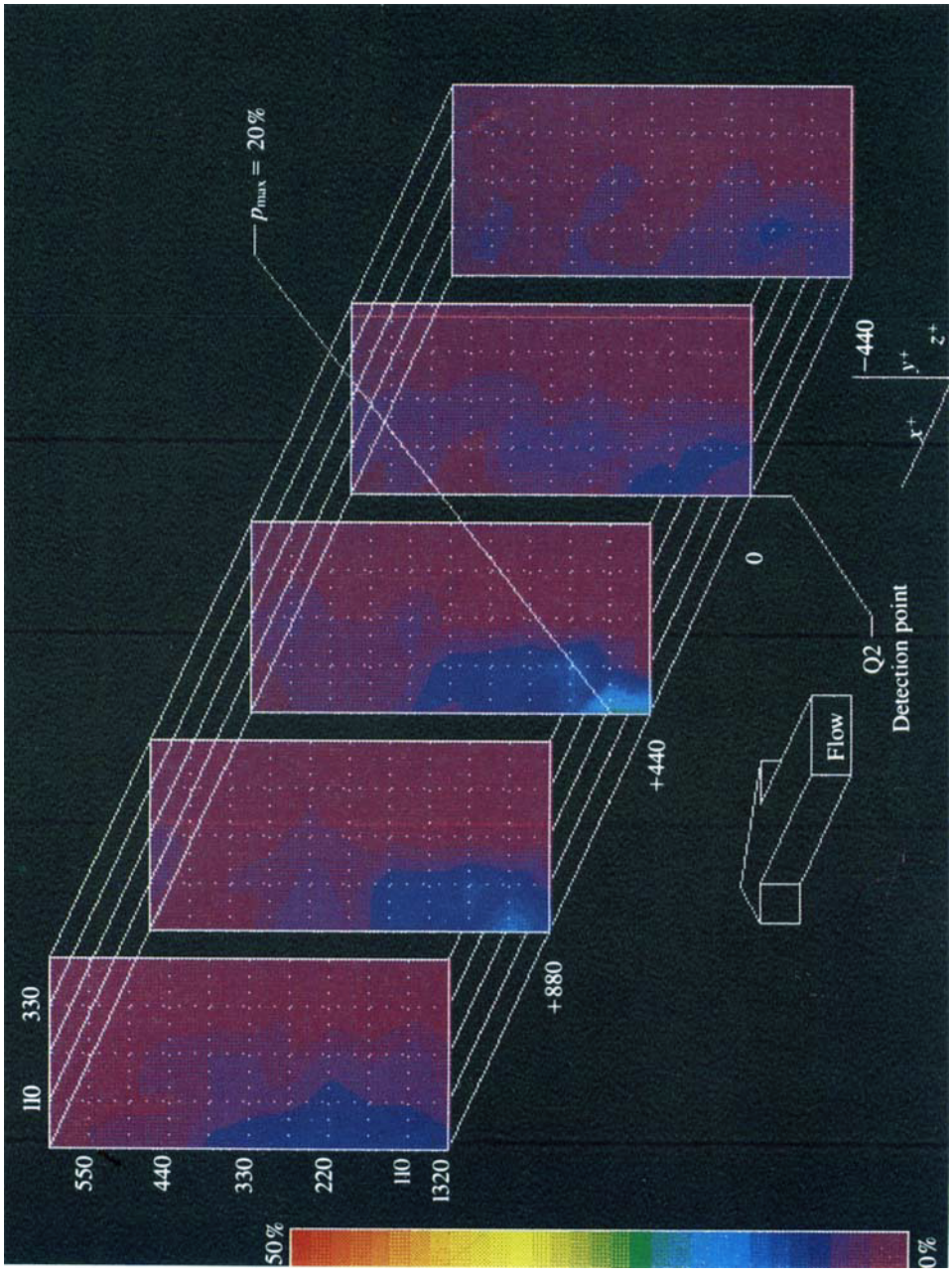


FIGURE 15. Spatial representation of the probability of observing a Q2 event ($k_Q$=0) $30t^+$ after the detection of a Q2 event at (0,35,0). $Re_\theta$ = 4650.

probability was assigned to a colour level as defined by the colourbar on each of figures 13–15 (plates 1–3).

Only data on one side of the detection point are shown. For each $(y^+, z^+)$-plane the intersections of the dotted lines are the measurement locations: linear interpolation provides the grey levels between the measurement locations. The magnitude of the maximum probability ($p_{\max}$) is given on each plot. For the Q4 (figures 13 and 14) detection scheme, three-dimensional p.d.f. distributions are shown for times corresponding to $-30$ and 30 wall time units with respect to time of detection. For the Q2 (figure 15) event, only results at $t^+ = 30$ will be shown.

Figure 13 represents a Q4 detection at $t^+ = -30$. The maximum probability of 32% is found upstream of the detection point at $x^+ = -440$. Significant levels of probability extend high into the boundary layer (for this $Re_\theta = 4650$, $y^+ = 605 \approx 0.4\delta$). For $t^+ = 30$ (figure 14) the maximum probability of 38% is found at $x^+ = 440$.

A similar trend with $t^+$ is noticed for a Q2 detection; however, only $t^+ = 30$ is shown. For $t^+ = 30$ the maximum probability is found at $x^+ = 440$ (figure 15) and is 20%. As shown by comparing figure 14 with figure 15, the maximum probabilities for a Q2 detection are considerably less than those for a Q4 detection. Also the spatial extent of a correlated region is less for a Q2 detection as compared with a Q4 detection. Therefore, these results provide another explanation (in addition to the 'centring' issue) of why the velocity vectors for the ensemble-averaged structure for the Q4 event are larger than those for the Q2 structure. That is, the fact that for this Reynolds number, the hierarchy of Q4 events contain more larger scale structures than the hierarchy of Q2 events. These results are very significant if one compares the NASA/Ames direct numerical simulation results for a turbulent boundary layer with the present results. The direct numerical simulation results are at a very low Reynolds number and show that the Q2 and Q4 structures are comparable in size. Although the present paper is not concentrating on Reynolds-number effects this conclusion is very striking and deserves to be pointed out.

The convection speed ($U_c$) of an event which travels a distance of $x^+$ in a given time $t^+$ is determined by the relation $U_c/U_\infty = x^+ u_\tau / U_\infty t^+$. At $x^+ = -440$ a peak was observed for the sweep event at $t^+ \approx -25$ and for $x^+ = 880$ at $t^+ \approx 50$. Therefore the convection speed associated with the evolution of this peak through the measurement volume is approximately $0.67U_\infty$. This compares very well with the convection velocities determined from the space–time correlations (see table 1).

## 4. Discussion of results

### 4.1. *Quadrant detection results*

The ensemble-averaged, large-scale, roller-like structure associated with Reynolds-stress production at the wall, extends several $\delta$ in the streamwise direction and to over $0.5\delta$ in both the vertical and spanwise directions. The magnitude of the velocity vectors for the coherent structures associated with an ejection of fluid from the wall are less than those associated with a sweep of fluid towards the wall (figures 7 and 8). Nevertheless, the average spanwise extent for both structures is equivalent (figure 9).

This is explained by the three-dimensional probability density distributions of figures 13–15. The three-dimensional p.d.f.'s are in essence a pseudo-instantaneous representation of the flow field during detection of strong Reynolds-stress production at $(x^+, y^+, z^+) = (0, 35, 0)$. The probabilities at the various points in the measurement

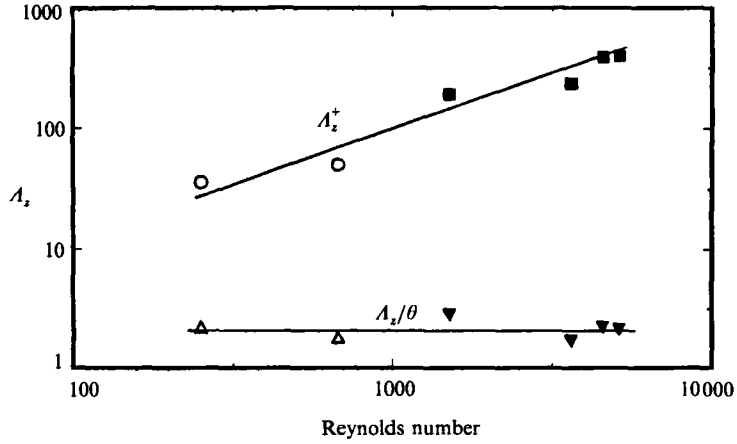


FIGURE 16. Scaling of an integral lengthscale of quadrant detected events: ○, △, NASA computations; ■, ▼, IIT experiments.

volume represent the percentage of time that a correlated Reynolds-stress-producing event extends from the detection point to the particular grid point. The three-dimensional p.d.f.'s therefore represent the distribution or hierarchy of scales associated with a quadrant detection.

The magnitudes of the Q2 velocity vectors (figure 8) are smaller than those for a Q4 event (figure 7) because the Q4 events have a greater percentage of relatively larger-scale structures: this is seen by comparing figures 13 and 14 with figure 15. The distribution of scales associated with an ejection or a sweep is much larger than that shown by the direct numerical simulation results from the NASA Ames/Stanford group (see Wark *et al.* 1991). This is illustrated by the results presented in figure 16. The integral lengthscale ($\Lambda_z$) of the ensemble-averaged structure, as defined in figure 9, is normalized using both inner-wall and outer-layer variables and plotted as a function of Reynolds number. The direct numerical simulation results (open symbols) are from Guezennec, Piomelli & Kim (1988), the experimental result at $Re_\theta \approx 1500$ is from Naguib (1989), the present result is shown at $Re_\theta = 4650$ and those at $Re_\theta \approx 3000$ and 5200 are from Nagib, Wark & Guezennec (1987). It is clear that inner scaling does not provide a collapse of $\Lambda_z^+$ with Reynolds number; however, $\Lambda_z/\theta$ appears to be insensitive to the Reynolds number. The growth of the structures with Reynolds number could be explained by the model proposed by Wark & Nagib (1989) discussed earlier.

As explained in the Introduction, the bursting frequency has been shown by many investigations to scale with inner-layer variables: some discrepancy does exist regarding this issue. Alfredsson & Johansson (1984) and more recently Shah & Antonia (1989) find that mixed scaling collapses their burst frequency results better than inner scaling. The key point here is that the discrepancy is between inner and mixed scaling and there is a consensus that outer scaling is *not* the appropriate scaling for collapsing burst frequency. However, the sizes and convection speeds of the larger scales in the hierarchy scale with the outer scales of the boundary layer. This suggests that the inner layer is responsible for the initiation of the production process; however, the associated scales gradually grow to sizes scaling with the outer layer.

Based upon the results of figure 9 a quasi-periodicity of Q2 and Q4 events in the spanwise direction is seen. The decrease in the magnitudes of the average

perturbation velocities, $\bar{u}$ and $\bar{v}$, indicate that the structures sitting next to the detected structures are not as strong (as determined by $k_Q$) and/or they only coexist for a certain percentage of the time. The indication at the present time is that both factors contribute to the decreased magnitude for $\bar{u}$ and $\bar{v}$: further discussion on this is given in Wark (1988) and Naguib (1989). The quasi-periodicity results are consistent with those of Robinson, Kline & Spalart (1988).

### 4.2. *Relation to space–time correlations*

The importance of the large-scale coherent structures can also be argued in the light of the non-conditioned space–time correlations presented in figures 3–6. The large degree of similarity between the space–time correlations and the ensemble-averaged results lend support to the argument that these structures are the dominant coherent structures of the boundary layer. The fact that they occur so infrequently in absolute terms, yet dominate the long-time correlations is very significant. The similarities between the conditional events and the long-time correlations are discussed below.

The magnitudes of the $R_{\tau_x u}$ correlations at $z^+ = 0$ decay slowly with increasing streamwise distance as seen in figure 3: this is consistent with the p.d.f. distributions of figures 13–15. The convection speed based upon the $t^+$ value for which the correlation is a maximum was observed to be approximately equal to $0.74U_\infty$ and $0.67U_\infty$ (table 1) (averaged over $y^+$) for the $R_{\tau_x u}$ and $R_{vv}$ correlations respectively. Consistent with this, the convection velocity estimated from the p.d.f. distribution for the Q4 event is approximately equal to $0.67U_\infty$. This is in good agreement with the estimates of $U_c$ for the sweep event given by Guezennec (1985) and Naguib (1989). No estimate of $U_c$ for the ejection event is given for the present results but can be found in Guezennec (1985) and Naguib (1989).

It is very plausible that the sweep motions are the significant contributor to the space–time correlations since the present results show that the Q4 hierarchy has more larger-scale structures than the Q2 hierarchy. Therefore, since the Q4 structures have, by definition, a streamwise velocity component greater than the local mean, it is entirely possible that the convection velocity is greater than the local mean as the results presented in figure 5(*c*) illustrate. The hierarchy of structures also aids in explaining the result first introduced in §3.2; that is, $U_c$ increases with increasing $y^+$. The explanation is that smaller scales in the hierarchy are the main contributor to the convection velocity results for the smaller $y^+$ values presented, and the larger scales dominate the $U_c$ results for the relatively larger $y^+$ values.

The spanwise distribution of $R_{\tau_x u}$ is very similar to that for the large-scale coherent structures. The magnitude of $\hat{R}_{\tau_x u}(x^+ = 0, y^+, z^+, t^+)$ decreases significantly from $z^+ = 0$ (figure 3*b*) to $z^+ = 220$ (figure 6). The decrease is observed until $z^+ = 440$ (not shown) where a slight dip towards negative values of $R_{\tau_x u}$ is observed. These trends are in excellent agreement with the ensemble-averaged conditional events; namely, the average streamwise perturbation velocity associated with these events (figure 9) changes sign at $z^+ = 385$.

## 5. Conclusions

By constructing pseudo-instantaneous conditional probability density distributions at all sampling points, it was conclusively demonstrated that a significant fraction of the individual events correlated with the Reynolds-stress production are relatively large in scale. The structures associated with sweeps of fluid towards the wall were found to be larger in scale than those associated with ejections of fluid away

from the wall. The larger scales were found to extend outward to $y^+ > 400$, have a spanwise extent on the order of 600 wall units, and persist for several $\delta$ in the streamwise direction. Sweeps and ejections of fluid were shown to occur side by side indicating a quasi-periodicity in the spanwise direction of Reynolds-stress-producing events. This quasi-periodicity is most significant to the phenomenological models of wall layers. The three-dimensional representation of the probability density distributions further points to a hierarchy of scales associated with the Reynolds-stress production process.

The results suggest a direct link between the space–time correlations and the quadrant-detected coherent structures. Specifically, the convection velocities inferred from both the long-time correlations and the conditional probability density functions are consistent. They were determined to convect at speeds slightly greater than the local mean velocity. This fact also illustrates the dominance of the sweep events compared with the ejection events in the space–time correlations. More importantly, the frequency of occurrence of these events is relatively small; however, the long-time correlations are dominated by the influence of the structures.

The scaling of the bursting frequency with inner-layer variables and the integral lengthscale of the larger structures involved in the hierarchy of scales with outer-layer variables, suggest that these scales are generated by a wall-layer mechanism but a significant fraction of them gradually develop to sizes and convect with velocities scaling with the outer layer.

The continuing support of this research by AFOSR under the direction of Dr J. McMichael is sincerely appreciated.

## REFERENCES

ALFREDSSON, P. H. & JOHANSSON, A. V. 1984 Time scales in turbulent channel flow. *Phys. Fluids* **27**, 1974–1981.

BAKEWELL, H. P. & LUMLEY, J. L. 1967 Viscous sublayer and adjacent region in turbulent pipe flow. *Phys. Fluids* **10**, 1880–1889.

BLACKWELDER, R. F. & ECKELMANN, H. 1979 Streamwise vortices associated with the bursting phenomenon. *J. Fluid Mech.* **94**, 577–594.

BLACKWELDER, R. F. & HARITONIDIS, J. H. 1983 Scaling of the bursting frequency in turbulent boundary layers. *J. Fluid Mech.* **132**, 87–103.

BLACKWELDER, R. F. & KAPLAN, R. E. 1976 On the wall structure of the turbulent boundary layers. *J. Fluid Mech.* **76**, 89–112.

BLACKWELDER, R. F. & KOVASNAY, L. S. G. 1972 Time scales and correlations in a turbulent boundary layer. *Phys. Fluids* **15**, 1545–1554.

BOGARD, D. G. & TIEDERMAN, W. G. 1986 Burst detection with single-point velocity measurements. *J. Fluid Mech.* **162**, 389–413.

BRODKEY, R. S., WALLACE, J. M. & ECKELMANN, H. 1974 Some properties of truncated turbulence signals in bounded shear flows. *J. Fluid Mech.* **63**, 209–224.

CHEN, C. H. P. & BLACKWELDER, R. F. 1978 Large scale motion in a turbulent boundary layer: a study using temperature contamination. *J. Fluid Mech.* **89**, 1–31.

CORINO, E. R. & BRODKEY, R. S. 1969 A visual investigation of the wall region in turbulent flows. *J. Fluid Mech.* **37**, 1–30.

GUEZENNEC, Y. G. 1985 Documentation of large coherent structures associated with wall events in turbulent boundary layers. Ph.D. thesis, Illinois Institute of Technology.

GUEZENNEC, Y. G. & NAGIB, H. M. 1990 Drag reduction in turbulent boundary layers. *AIAA J.* **28**, 245–252.

GUEZENNEC, Y. G., PIOMELLI, U. & KIM, J. 1987 Conditionally-averaged structures in wall-

bounded turbulent flows. In *Proc. 1987 Summer Program, Center for Turbulence Research, Stanford, CA*, pp. 263–272.

HEAD, M. R. & BANDYOPADHYAY, P. 1981 New aspects of turbulent boundary-layer structure. *J. Fluid Mech.* **107**, 297–337.

JOHANSSON, A. V., ALFREDSSON, P. H. & KIM, J. 1987 Shear-layer structures in near-wall turbulence. In *Proc. 1987 Summer Program, Center for Turbulence Research, Stanford, CA*, pp. 237–251.

KASAGI, N., HIRATA, M. & NISHION, K. 1986 Streamwise pseudo-vortical structures and associated vorticity in the near-wall region of a wall-bounded turbulent shear flow. *Exps Fluids* **4**, 309–318.

KIM, H. T., KLINE, S. J. & REYNOLDS, W. C. 1971 The production of turbulence near a smooth wall in a turbulent boundary layer. *J. Fluid Mech.* **50**, 133–160.

KIM, J. 1985 Turbulence structure associated with the bursting event. *Phys. Fluids* **28**, 52–58.

KIM, J. & SPALART, P. R. 1987 Scaling of the bursting frequency in turbulent boundary layers at low Reynolds numbers. *Phys. Fluids* **30**, 3326–3328.

KLINE, S. J., REYNOLDS, W. C., SCHRAUB, F. A. & RUNSTADLER, P. W. 1967 The structure of turbulent boundary layers. *J. Fluid Mech.* **30**, 741–773.

KREPLIN, H. P. & ECKELMANN, H. 1979 Propagation of perturbations in the viscous sublayer and adjacent wall region. *J. Fluid Mech.* **95**, 305–322.

LU, S. S. & WILLMARTH, W. W. 1973 Measurements of the structure of the Reynolds stress in a turbulent boundary layer. *J. Fluid Mech.* **60**, 481–511.

LUCHIK, T. S. & TIEDERMAN, W. G. 1987 Timescale and structure of ejections and bursts in turbulent channel flows. *J. Fluid Mech.* **174**, 529–552.

NAGIB, H. M. & GUEZENNEC, Y. G. 1986 On the structure of turbulent boundary layers. *Proc. 10th Symp. on Turbulence, Rolla Missouri.*

NAGIB, H. M., WARK, C. E. & GUEZENNEC, Y. G. 1987 Documentation of turbulence producing structures in regular and manipulated turbulent boundary layers. In *Proc. the IUTAM Symp. on Turbulence Management and Relaminarisation. Bangalore, India, Paper* 1. Springer.

NAGUIB, A. M. 1989 Reynolds number effect on the scales and symmetry of coherent structures in a turbulent boundary layer. M.S. thesis, Illinois Institute of Technology.

PERRY, A. E. & CHONG, M. S. 1982 On the mechanisms of wall turbulence. *J. Fluid Mech.* **119**, 173–217.

PERRY, A. E., HENBEST, S. & CHONG, M. S. 1986 A theoretical and experimental study of wall turbulence. *J. Fluid Mech.* **165**, 163–199.

PLESNIAK, M. W. 1985 Optimized manipulation of turbulent boundary layers aimed at net drag reduction. M.S. thesis, Illinois Institute of Technology.

RAO, K. N., NARASIMHA, R. & NARAYANAN, M. A. 1971 The 'bursting' phenomenon in a turbulent boundary layer. *J. Fluid Mech.* **48**, 339–352.

RAUPACH, M. R. 1981 Conditional statistics of Reynolds stress in rough-wall and smooth-wall turbulent boundary layers. *J. Fluid Mech.* **108**, 363–382.

ROBINSON, S. K., KLINE, S. J. & SPALART, P. R. 1988 Quasi-coherent structures in the turbulent boundary layer: Part II. Verification and new information from a numerically simulated flat-plate layer. In *Proc. Zoran Zaric Memorial Seminar on Near-Wall Turbulence, Dubrovnik, Yugoslavia, May 1988.*

SHAH, D. A. & ANTONIA, R. A. 1989 Scaling of the 'bursting' period in turbulent boundary layer and duct flows. *Phys. Fluids* A **1**, 318–325.

SMITH, C. R. & METZLER, S. P. 1983 The characteristics of low-speed streaks in the near wall region of a turbulent boundary layer. *J. Fluid Mech.* **129**, 27–46.

SMITH, C. R. & SCHWARTZ, S. P. 1983 Observation of streamwise rotation in the near-wall region of a turbulent boundary layer. *Phys. Fluids* **26**, 641–652.

SREENIVASAN, K. R. 1987 A unified view of the origin and morphology of the turbulent boundary layer structure. In *Proc. IUTAM Symp. on Turbulence Management and Relaminarisation, Bangalore, India.* Springer.

WALLACE, J. M., ECKELMANN, H. & BRODKEY, R. S. 1972 The wall region in turbulent shear flow. *J. Fluid Mech.* **54**, 39–48.

WARK, C. E. 1988 Experimental investigation of coherent structures in turbulent boundary layers. Ph.D. thesis, Illinois Institute of Technology.

WARK, C. E. & NAGIB, H. M. 1988 Scaling of frequency of Reynolds-stress producing events in regular and manipulated boundary layers. In *Proc. Zoran Zaric Memorial Seminar on Near-Wall Turbulence, Dubrovnik, Yugoslavia.*

WARK, C. E. & NAGIB, H. M. 1989 Relation between outer structures and wall-layer events in boundary layers with and without manipulation. In *Proc. 2nd IUTAM Symp. on Structure of Turbulence and Drag Reduction, Zurich, Switzerland, July 1989.*

WARK, C. E., ROBINSON, S. K., NAGUIB, A. M. & SPALART, P. R. 1991 Scaling of spanwise length scales in a turbulent boundary layer. *29th Aerospace Science Meeting, Reno, Nevada.*

WILLMARTH, W. W. & SHARMA, L. K. 1984 Study of turbulent structure with hot wires smaller than the viscous length. *J. Fluid Mech.* **142**, 121–149.